ADVANCED SENSOR RESEARCH Open Access
www.advsensorres.com

Modeling of High-Sensitivity SAW Magnetic Field Sensors with Au-SiO_2 Phononic Crystals

Mohsen Samadi, Jana Marie Meyer, Elizaveta Spetzler, Benjamin Spetzler, Jeffrey McCord, Fabian Lofink, and Martina Gerken**

The development of high-sensitivity magnetic field sensors is crucial for precise magnetic field detection. In this context, a theoretical model is presented for a highly sensitive surface acoustic wave (SAW) magnetic field sensor incorporating phononic crystal (PnC) structures composed of Au pillars embedded within a SiO_2 guiding layer. Rectangular and triangular PnC configurations are studied and their potential for improving sensor performance are assessed. In the design, the PnC is integrated into the SiO_2 guiding layer to preserve the continuous magnetostrictive layer, enhancing its interaction with the SAW. Results from the simulations indicate that the proposed sensor can achieve a nearly two orders of magnitude increase in sensitivity compared to a continuous delay line of similar dimensions, and an eightfold improvement over a previous sensor design with PnCs composed of magnetostrictive pillars. This improved performance is attributed to the enhanced interaction between the SAW and the continuous magnetostrictive layer, driven by resonance effects within the PnC. These findings highlight the significant potential of incorporating PnCs into SAW sensors for future high-performance magnetic field sensing.

1. Introduction

Magnetic field sensors are essential tools for detection and accurate measurement of magnetic fields in various applications.[1–11] In particular, magnetic field sensors based on surface acoustic waves (SAW)[12–15] have been employed to detect minute changes in magnetic field through the ΔE effect, where the stiffness tensor of a magnetostrictive material changes in response to an external magnetic field.[16–20] This change induces modulation in the SAW phase, which is measured to determine the magnetic field strength.[21–25]

Unlike sensing approaches based on magnetoelectric cantilevers, which are limited by narrow bandwidths ranging from a few hertz to a few kHz,[26–28] SAW-based magnetic field sensors can detect small amplitude magnetic fields over a broader frequency range.[21–24] Recently, detection limits of 2.4 $nT/Hz^{1/2}$ at 10 Hz and 72 $pT/Hz^{1/2}$ at 10 kHz were experimentally achieved with a thin-film SAW magnetic field sensor, highlighting the potential of this configuration for highly sensitive magnetic field detection.[25] The sensor utilized a thin film of aluminum scandium nitride (AlScN) as the piezoelectric material on a silicon substrate. A SiO_2 layer was deposited onto the AlScN layer to confine acoustic waves near the surface, minimizing energy loss into the substrate and enhancing the interaction between the SAW and the magnetostrictive material. Additionally, the SiO_2 layer was polished using chemical mechanical polishing method to create a smooth surface for the deposition of

M. Samadi, M. Gerken
Integrated Systems and Photonics
Department of Electrical and Information Engineering
Kiel University
Kaiserstraße 2, 24143 Kiel, Germany
E-mail: mosa@tf.uni-kiel.de; mge@tf.uni-kiel.de

J. M. Meyer, F. Lofink
Fraunhofer Institute for Silicon Technology ISIT
Fraunhoferstraße 1, 25524 Itzehoe, Germany

E. Spetzler, J. McCord
Nanoscale Magnetic Materials – Magnetic Domains
Department of Materials Science
Kiel University
Kaiserstraße 2, 24143 Kiel, Germany

B. Spetzler
Energy Materials and Devices
Department of Materials Science
Kiel University
Kaiserstraße 2, 24143 Kiel, Germany

J. McCord, F. Lofink, M. Gerken
Kiel Nano, Surface and Interface Science (KiNSIS)
Kiel University
Kaiserstraße 2, 24143 Kiel, Germany

F. Lofink
Microsystem Materials
Department of Materials Science
Kiel University
Kaiserstraße 2, 24143 Kiel, Germany

The ORCID identification number(s) for the author(s) of this article can be found under https://doi.org/10.1002/adsr.202500008

DOI: 10.1002/adsr.202500008

the magnetostrictive FeCoSiB film, improving its soft magnetic properties.

Compared to bulk piezoelectric substrates such as quartz[22] and $LiNbO_3$,[29] which are commonly used, thin-film SAW configurations offer reduced chip sizes and improved functionality, providing a more compatible solution for complementary metal-oxide semiconductor (CMOS) and micro-electromechanical system (MEMS) technologies.[30] Thin-film Aluminum Nitride (AlN) is recognized as a highly promising piezoelectric material due to its high acoustic wave velocity, thermal stability, and CMOS compatibility enabled by low-temperature deposition.[31–35] Alloying AlN with transition metals such as scandium improves its electromechanical coupling, making it particularly suitable for high-frequency applications.[36,37]

SAWs can drive magnetization dynamics in ferromagnetic materials through spin-phonon coupling, a process enabled by SAW-driven ferromagnetic resonance.[38–41] This phenomenon allows for control over both spin and SAW dynamics, giving rise to effects such as nonreciprocity of SAWs.[42–46] Periodic structures further provide precise control over wave propagation and dispersion. For instance, photonic crystals manipulate electromagnetic waves to create peculiar phenomena such as photonic bandgaps,[47–49] resonant field enhancement and localization,[50–52] and slow-light effects,[53–55] which have been leveraged to achieve high sensitivities in PhC-based sensors.[56–58] Similarly, phononic[59] and magnonic[60] crystals enable the control of acoustic and spin waves, respectively. The ability to manipulate waves has made these periodic structures a powerful tool for improving sensor sensitivity by facilitating strong wave localization and enhancing wave-material interactions.

Phononic crystals (PnCs) are periodic structures composed of two materials with different acoustic impedance values.[59,61–64] By tailoring the geometry and material composition of PnCs, precise control over the propagation and dispersion of acoustic waves can be achieved.[65,66] A prior study[67] demonstrated that integrating carefully designed PnCs into SAW magnetic field sensors significantly enhances their sensitivity to magnetic field variations. The PnC structure consisted of a 2D square array of FeCoSiB pillars deposited onto a SiO_2 guiding layer. Nevertheless, patterning the magnetostrictive layer results in a considerable material loss, thereby reducing the interaction between the SAW and the magnetostrictive material.

In this groundbreaking study, adopting a configuration similar to that proposed in our previous research,[25] we leverage the remarkable piezoelectric properties of AlScN thin films with an integrated PnC structure to present a design and theoretical model for a thin-film SAW magnetic field sensor with a drastically improved sensitivity. The PnC consists of a 2D lattice of Au pillars embedded within a SiO_2 guiding layer, topped with a continuous layer of magnetostrictive material. The resonant SAWs propagate through the PnC, confined to the top surface of the guiding layer that surrounds the PnC, thereby strongly enhancing the interaction with the unpatterned magnetostrictive layer.

We evaluate the changes in the stiffness tensor of the magnetostrictive layer in response to small magnetic field variations using a magnetoelastic macrospin model. The resulting data is then used as input for the electromechanical model to estimate changes in the phase velocity of the PnC modes and assess the sensor's sensitivity. Through precise alignment of the PnC resonant modes with the frequency of the input SAW, we demonstrate that a small change in the applied magnetic field results in a substantial change in the phase velocity, yielding remarkably high sensitivity.

The paper is structured as follows. Section 2 introduces the novel sensor design, explaining the thin-film configuration and the PnC structure. Section 3 describes the theoretical model, focusing on the electromechanical and magnetoelastic models as well as the sensor's sensitivity. Section 4 presents the results, divided into subsections that examine the band structures of the PnCs, the displacement of SAWs through the PnCs, and the use of the ΔE effect as a mechanism for magnetic field detection. In section 5 the results are discussed in a bigger picture. Finally, the improvements in comparison to existing structures are highlighted in section 6.

2. Sensor Design

Figure 1a,b schematically display the 3D and cross-sectional views of the sensor. A thick silicon substrate is coated by a 1 µm-thick AlScN piezoelectric layer. Two interdigital transducers (IDT) are devised on the AlScN layer to generate and detect a Rayleigh wave at a center frequency of $f = 250$ MHz. A SiO_2 layer is deposited onto the piezoelectric layer acting as a guiding medium for the SAW. A rectangular or triangular lattice of Au pillars is embedded within the SiO_2 guiding layer between the two IDTs, as illustrated in Figure 1c,d. The pillars are of the same thickness as the guiding layer ($h_p = h_{GL} = 4.5$ µm). The entire PnC structure is then covered by a continuous magnetostrictive FeCoSiB layer with a thickness of $h_{MS} = 200$ nm.

The top views of the rectangular and triangular PnCs are depicted in Figure 1c,d. Rectangular supercells, marked by dashed boxes, were selected in both configurations to calculate the PnC band structures. This approach enables the construction of the complete structures by repeating the supercells along the *x*- and *y*-axes. To ensure a valid comparison, the primary lattice constant *a*, defined as the distance between the nearest-neighbor pillars along the *x*-axis, is identical in both PnCs. The secondary lattice constant *b* along the *y*-axis was defined as $b = 2aq$ for the rectangular PnC and $b = \sqrt{3}\,aq$ for the triangular PnC. Here, the tuning coefficient *q* adjusts the lateral spacing between pillars relative to their longitudinal distance to maximize sensitivity.

The main focus of this study is the design and theoretical modeling of a SAW magnetic field sensor with integrated PnCs to enhance sensitivity. However, a feasible fabrication process has also been outlined based on the design parameters obtained from simulations and is currently in progress. The fabrication process begins with the sputtering of an AlScN layer onto a silicon wafer. For the IDTs and the plating base, WTi/Au is sputtered and structured using wet chemical etching. The SiO_2 guiding layer is then deposited using plasma-enhanced chemical vapor deposition and patterned to create holes matching the dimensions of the designed PnC pillars. Next, an electroplating process is used to fill the structured holes with Au, forming the PnC pillars. A thin passivation layer of SiO_2 is then deposited using PECVD and smoothed via chemical mechanical polishing. Finally, the FeCoSiB magnetostrictive layer is sputtered onto the PnC, completing the fabrication process.

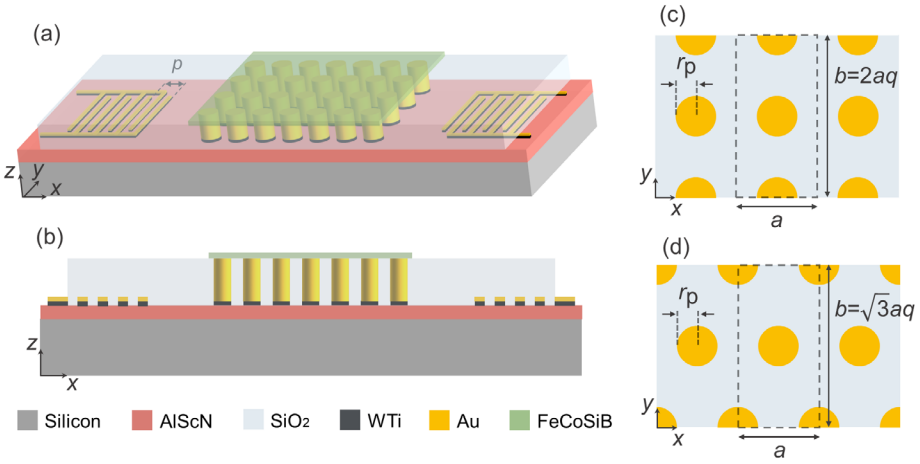

Figure 1. a) 3D and b) cross-sectional view of the SAW magnetic field sensor with Au-SiO_2 PnC. A rectangular or triangular lattice of Au pillars is patterned within a SiO_2 guiding layer to build a PnC between the IDTs. Top views of the c) rectangular and d) triangular PnCs. Rectangular super cells of the two PnCs are indicated by dashed lines. *a* and *b* denote the lattice constants of the PnCs along the *x*- and *y*-axis, while r_p represents the radius of the pillars.

3. Theoretical Model

3.1. Equation System

The sensor's electromechanical response is characterized by solving a set of coupled differential equations through the finite element method. The equation of motion relates the displacement vector $\mathbf{u}$ to the divergence of the mechanical stress tensor $\boldsymbol{\sigma}$:[68,69]

$$\nabla \cdot \boldsymbol{\sigma} = -\rho\omega^2\mathbf{u} \tag{1}$$

Here, ρ and ω are the mass density and the angular frequency, respectively. Assuming that free charges and eddy currents are negligible, Maxwell's electrostatic equation is expressed as[70]

$$\nabla \cdot \mathbf{D} = 0 \tag{2}$$

where $\mathbf{D}$ represents the electric flux density vector. The electric field vector $\mathbf{E}$ is derived from the gradient of the electric potential V:

$$\mathbf{E} = -\nabla V \tag{3}$$

The mechanical equation of motion (Equation (1)) is coupled to the electrostatic equation (Equation (2)) through the constitutive piezoelectric equations in the stress-charge form:[70,71]

$$\boldsymbol{\sigma} = \mathbf{C}\boldsymbol{\varepsilon} - \mathbf{e}^{\mathrm{T}}\mathbf{E} \tag{4}$$

$$\mathbf{D} = \mathbf{e}\boldsymbol{\varepsilon} - \boldsymbol{\varepsilon}_{\mathrm{el}}\mathbf{E} \tag{5}$$

In these equations, $\boldsymbol{\epsilon}$ is the strain tensor, $\mathbf{C}$ is the mechanical stiffness tensor, while $\mathbf{e}$ and $\boldsymbol{\epsilon}_{\mathrm{el}}$ denote the piezoelectric coupling and electrical permittivity tensors, respectively.

3.2. Modeling Approach

To investigate the ΔE effect, we employed a semi-analytical magnetoelastic macrospin model to estimate the magnetic field-dependent stiffness tensor of FeCoSiB. Details of this approach are provided in another study.[20] The resulting magnetic field-dependent stiffness tensor was then used in Equation (4), as input to the electromechanical model developed in COMSOL Multiphysics[72] to simulate the sensor's response. The material parameters used in the magnetoelastic model are given in Appendix A.

We employed COMSOL Multiphysics to calculate the band structures of the PnCs, limiting our analysis to a single supercell, as indicated by the dashed rectangles in Figure 1c,d, to save time and computational resources. Bloch-Floquet boundary conditions were applied at the supercell boundaries to simulate infinite periodicity in both *x* and *y* directions.[64,73] By varying the wavevector along the Γ-X direction of the first Brillouin zone and solving the eigenvalue problem, we obtained the eigenfrequencies for each wavevector. These eigenfrequencies indicate the acoustic modes permitted to propagate through the PnCs.

Moreover, we modeled PnCs with a finite number of periodicities ($n = 20$) integrated into the delay line of a SAW magnetic field sensor. We applied an alternating voltage to an IDT to generate a Rayleigh wave with a specific center frequency. The PnC parameters were carefully designed to align a PnC mode with the Rayleigh wave generated by the IDT. We calculated the average displacement across the top surface of the PnCs, which was coated with an FeCoSiB layer, at different frequencies. To model infinite periodic repetitions and sufficiently long IDT fingers, we applied a periodic boundary condition along the *y*-axis. Additionally, perfectly matched layers were imposed in both the *x* and *z* directions to prevent unwanted reflections from the domain boundaries.

3.3. Sensor's Sensitivity

Magnetic sensitivity describes the variation in the stiffness tensor of the magnetostrictive layer in response to changes in the applied magnetic field magnitude. At a specific bias magnetic field magnitude $|H| = H_0$, a small field variation ΔH induces a

change in the stiffness tensor **C** of the magnetostrictive material. Since different components of the stiffness tensor **C** exhibit distinct responses to the applied magnetic field, magnetic sensitivity is defined by a tensor $\mathbf{S}_{mag}$ of the same order and dimensions as **C**. Each component of the magnetic sensitivity tensor represents the rate of change of its corresponding stiffness tensor component with respect to the magnetic field magnitude $|H|$, expressed as $S_{mag,ij} = \partial C_{ij}/\partial|H|$.

Structural sensitivity quantifies how changes in the stiffness tensor **C** induced by the magnetic field affect the SAW velocity v. It is strongly influenced by the design of the delay line through which the wave propagates. For instance, increasing the thickness of the guiding layer beneath the magnetostrictive material in a delay line configuration has been shown to enhance the structural sensitivity.[21] Additionally, a recent study demonstrated that the structural sensitivity of a SAW magnetic field sensor can be improved by replacing the continuous magnetostrictive layer with a periodic array of magnetostrictive pillars, forming a PnC.[67] The SAW velocity v is influenced differently by each component of the stiffness tensor **C**. Therefore, structural sensitivity is expressed as a tensor $\mathbf{S}_{str}$ of the same order and dimensions as **C**, with each component $S_{str,ij} = \partial v/\partial C_{ij}$ representing the derivative of the SAW velocity with respect to the corresponding components of the stiffness tensor.

The combined effect of the magnetic and structural sensitivity is represented by a scalar value, referred to as the magneto-structural sensitivity, $S_{mag-str}$. This scalar quantifies how the SAW velocity varies in response to changes in the magnetic field magnitude. It is calculated by summing the products of the corresponding components of the two sensitivity tensors, $\mathbf{S}_{mag}$ and $\mathbf{S}_{str}$, over all indices:

$$S_{mag-str} = \frac{\partial v}{\partial |H|} = \sum_{i,j} S_{mag,ij} \cdot S_{str,ij} \tag{6}$$

where $S_{mag,ij}$ and $S_{str,ij}$ denote the components of the magnetic and structural sensitivity tensors and the summation is performed over all indices i and j.

The phase φ of a SAW with a frequency f and a velocity v, detected at the end of a delay line of length l, is given by:

$$\varphi = 2\pi f \frac{l}{v} \tag{7}$$

At a fixed frequency, any change in the SAW velocity induces a phase delay in the output signal. The extent of this phase delay per unit changes in the SAW velocity, referred to as the geometric sensitivity S_{geo}, is expressed as:

$$S_{geo} = \frac{\partial \varphi}{\partial v} = -2\pi f \frac{l}{v^2} \tag{8}$$

The overall sensitivity of the sensor is determined by the product of the magneto-structural and geometric sensitivity, quantifying the sensor's output phase delay in response to changes in the magnetic field magnitude:

$$S = \frac{\partial \varphi}{\partial |H|} = \frac{\partial v}{\partial |H|} \cdot \frac{\partial \varphi}{\partial v} = S_{mag-str} \cdot S_{geo} \tag{9}$$

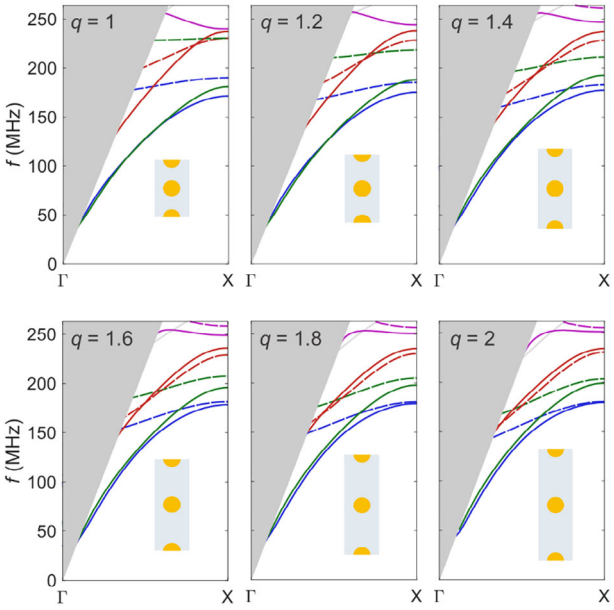

Figure 2. Band structures of the rectangular PnC, as illustrated in Figure 1c, with a = 6 µm, r_p = 1.5 µm, and different values of the tuning coefficient: q = 1, q = 1.2, q = 1.4, q = 1.6, q = 1.8 and q = 2. The lattice constant along the y-axis is expressed as $b = 2aq$ for the rectangular PnC. All diagrams were calculated along the Γ-X direction of the first Brillouin zone. The grey-shaded area outlines the sound cone. Insets display the top views of the rectangular supercells used to calculate the band structures.

4. Results

4.1. Band Structures of the PnCs

In this section, we calculate the band structures and analyze the dispersion characteristics of PnCs with either a rectangular or triangular arrangement of Au pillars embedded within a SiO_2 guiding layer, as depicted in Figure 1. Band diagrams of the rectangular and triangular PnCs with a = 6 µm, r_p = 1.5 µm, calculated along the Γ-X direction of the first Brillouin zone, are shown in **Figure 2** and S1 (Supporting Information), respectively. The gray-shaded area in the band diagrams represents the sound cone. Acoustic modes that lie within this cone radiate into the bulk material, whereas surface acoustic modes appear only outside the sound cone. The tuning coefficient is varied between q = 1 and q = 2 by a step size of 0.2, to investigate the effect of lateral distance between pillars with respect to their longitudinal distance.

To provide a clear understanding of each mode's characteristics, **Figure 3** presents the band diagram of a rectangular PnC with a fixed tuning coefficient of q = 2, with each mode labeled by a number. The displacement profile of each mode is displayed within a single supercell at a wavevector k near the edge of the first Brillouin zone. The band diagram and modal displacement profiles for a triangular PnC with a tuning coefficient of q = 2 are also presented in Figure S2 (Supporting Information). Based on the displacement profiles, lower-order modes exhibit mostly uniaxial oscillations, while higher-order modes induce combined longitudinal and vertical surface displacements. Modes 1 and 2

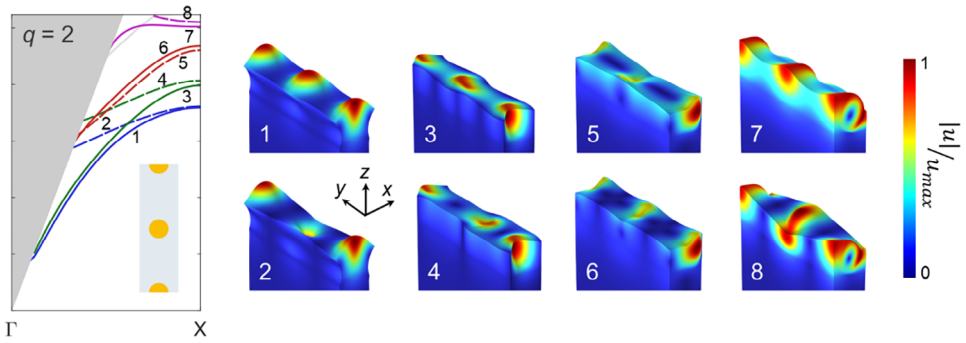

Figure 3. Band structure of the rectangular PnC with $a = 6$ µm, $r_p = 1.5$ µm, and $q = 2$, calculated along the Γ-X direction of the first Brillouin zone. Distinct surface acoustic modes are labeled by numbers, with corresponding normalized modal displacements ($|u|/u_{max}$) displayed within a single supercell at a wavevector k near the edge of the first Brillouin zone. Lower-order modes exhibit almost uniaxial oscillations: modes 1 and 2 (blue) along the z-axis, modes 3 and 4 (green) along the y-axis, and modes 5 and 6 (red) along the x-axis. In contrast, higher-order modes 7 and 8 (magenta) exhibit coupled longitudinal and vertical oscillations in the x-z plane.

(blue curves) oscillate vertically along the z-axis, whereas modes 3 and 4 (green curves) generate shear-horizontal displacements along the y-axis, representing Love modes. Modes 5 and 6 (red curves) primarily induce longitudinal displacements along the x-axis. In contrast, modes 7 and 8 (magenta curves) exhibit both longitudinal and vertical oscillations in the x-z plane, corresponding to Rayleigh modes. To enable SAW propagation through the PnC, it is essential that the selected PnC mode matches in both frequency and polarization with the Rayleigh wave launched by the IDT. In the current PnC configuration, Rayleigh waves are utilized due to their out-of-plane oscillations, which enable efficient coupling with the continuous FeCoSiB layer on top of the SiO_2 guiding layer, resulting in higher sensitivity. While Love waves could be explored as an alternative, their purely in-plane displacements pose challenges for efficient coupling with the top FeCoSiB layer in this specific design. Accordingly, the following sections of the paper focus on mode 7, a Rayleigh mode with a center frequency of ≈250 MHz.

Integrating PnCs into a SAW magnetic field sensor can significantly enhance its sensitivity. To demonstrate this, we compared the band diagram of a rectangular PnC with a tuning coefficient of $q = 2$ to that of a continuous guiding layer with similar dimensions, as shown in Figure S3 (Supporting Information). The band diagram of the continuous guiding layer was calculated using a supercell identical in dimensions to that in Figure 1c, but without Au pillars. The band diagram of the PnC exhibits nearly flat bands with extremely low group velocities near the edge of the first Brillouin zone (X point), in contrast to the continuous guiding layer, where surface acoustic modes appear as linear bands with a fixed group velocity for all wavevectors along the Γ-X direction. The slow-wave phenomenon in PnCs arises from the resonant coupling of local modes between neighboring pillars at specific frequencies, forming collective guided surface modes with reduced group velocity. This leads to an effectively longer interaction between the SAW propagating through the PnC and the continuous magnetostrictive layer covering the guiding layer's top surface. By fine-tuning the PnC design parameters, the edge of a PnC mode can be precisely aligned with the frequency of the input SAW generated by an IDT. Consequently, small changes in the magnetic field induce larger variations in the SAW phase velocity, significantly enhancing the sensor's sensitivity.

In both rectangular and triangular configurations, an increase in the tuning coefficient q, which corresponds to a larger lateral distance between the pillars relative to the longitudinal lattice constant a, reduces the slopes of all bands, including mode 7. To illustrate this effect, **Figure** 4a and S4a (Supporting Information) presents the dispersion curves of mode 7 near the edge of the first Brillouin zone for the rectangular and triangular PnCs, respectively. These curves are plotted for different values of the tuning coefficients: $q = 1$, $q = 1.2$, $q = 1.4$, $q = 1.6$, $q = 1.8$ and $q = 2$. From these dispersion curves, the group velocity ($v_g = 2\pi\frac{\partial f}{\partial k}$) of mode 7 was calculated at a certain wavenumber $k = 0.8\pi/a$ for each value of q. Figure 4b and S4b show the group velocity variations with q for the rectangular and triangular PnCs, respectively. In both configurations, a noticeable decrease in group velocity is observed as q increases. At $q = 2$, the group velocity reaches ≈100 m s^{-1} for the rectangular PnC and 150 m s^{-1} for the triangular PnC.

4.2. Displacement Across the PnCs

To model the propagation of SAWs through the PnCs, either a rectangular or triangular PnC with $a = 6$ µm, $r_p = 1.5$ µm, $q = 2$, and finite number of periodicities ($n = 20$) along the x-axis was integrated into the delay line of a SAW magnetic field sensor, as shown in **Figure** 5b and S5b (Supporting Information). A spatially alternating electric potential was applied to an IDT composed of 12 pairs of Au split-finger structures with a periodicity of 16 µm, a finger width of 4 µm, and a thickness of 150 nm to generate a Rayleigh wave with a center frequency of 250 MHz. The average displacement across the top surface of the PnCs, coated with an FeCoSiB layer, was then calculated at different frequencies. Without the PnCs, the average displacement spectrum features a broad, barely-visible peak centered ≈ 250 MHz (red curves in Figure 5a; Figure S5a, Supporting Information). However, when a PnC is integrated into the delay line, the average displacement spectra reveal sharp peaks, as shown by the blue curve in Figure 5a and the green curve in Figure S5a (Supporting Information). These sharp peaks at certain frequencies are attributed to resonance effects induced by the periodic arrangement of pillars within the PnCs. Maximum values of ≈0.11 and

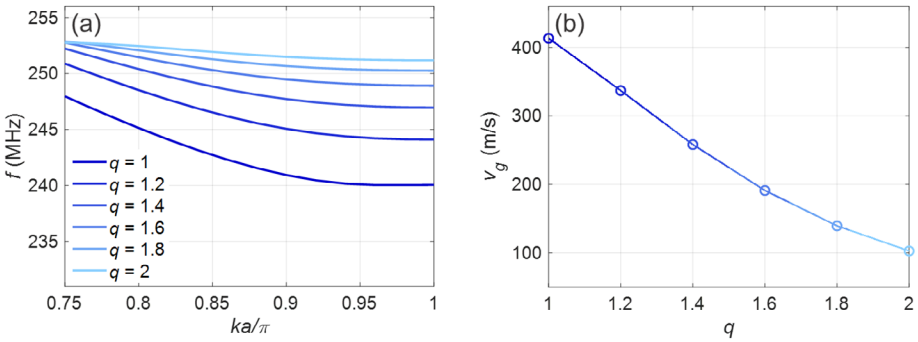

Figure 4. a) Dispersion curves of mode 7 near the edge of the first Brillouin zone for the rectangular PnC at different values of the tuning coefficients: $q = 1$, $q = 1.2$, $q = 1.4$, $q = 1.6$, $q = 1.8$ and $q = 2$. b) Group velocity variations with q for the rectangular PnC, calculated from the dispersion curves at $k = 0.8\pi/a$.

0.05 nm, per unit of the electric potential applied to the IDT, are achieved at the resonance frequencies of the rectangular and triangular PnCs, respectively. Figure 5b and Figure S5b (Supporting Information) depict the spatial displacement along each type of PnC at their respective resonance frequencies, showing that both PnCs allow Rayleigh waves to be resonantly guided, thereby amplifying oscillations across their top surfaces. At other frequencies, however, PnCs block the incoming Rayleigh wave, leading to minimal oscillations along the delay line.

4.3. ΔE Effect

We used the magnetoelastic macrospin model to calculate the stiffness tensor components of the FeCoSiB layer under various magnetic field strengths. We assumed that the applied magnetic field was oriented along the y-axis, aligned with the hard axis of the FeCoSiB layer. **Figure 6** presents the primary non-zero magnetic field-dependent components of the FeCoSiB stiffness tensor, i.e., C_{11}, C_{12}, C_{16} and C_{66}, along with the derivatives of each component with respect to the applied magnetic field. Other non-zero components are excluded, as they either depend on and can be derived from these four components ($C_{22} = C_{11}$, $C_{21} = C_{12}$, $C_{61} = C_{16}$, $C_{62} = C_{26} = -C_{16}$) or remain invariant under an in-plane magnetic field ($C_{13} = C_{31} = C_{23} = C_{32} = 86.54$ GPa, $C_{33} = 201.92$ GPa and $C_{44} = C_{55} = 57.69$ GPa).[20] These four components, along with their dependent components, exhibit significant variations with the applied magnetic field. Among them, C_{16} is zero in the absence of an external magnetic field (at $|H| = 0$). The other three components, C_{11}, C_{12}, and C_{66}, have non-zero baseline values at zero magnetic field, to which a field-dependent term, varying with magnetic field strength, is added.

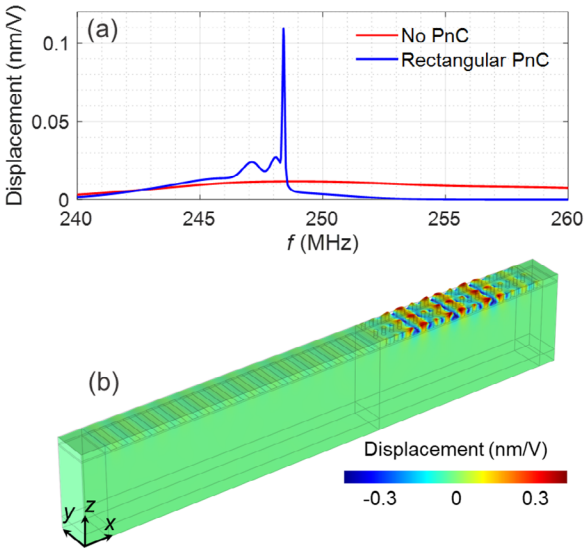

Figure 5. a) Average displacement spectra across the top surface of the delay line with the rectangular PnC with $a = 6$ µm, $r_p = 1.5$ µm, and $q = 2$ (blue curve). The average displacement spectra for a continuous delay line without PnC is also plotted for comparison (red curve). b) The spatial displacement along the rectangular PnC at its resonance frequency. The displacement values are normalized to the amplitude of the AC electric potential applied to the IDT. The PnC has 20 periodicities along the x-axis ($n = 20$) and the IDT comprises 12 pairs of Au split-finger structures with a periodicity of 16 µm, a finger width of 4 µm, and a thickness of 150 nm.

The magnetic sensitivity of each stiffness tensor component is highest when the derivative of that component with respect to the applied magnetic field magnitude, $\partial C_{ij}/\partial|H|$, is maximized. For our analysis, we selected a magnetic field magnitude of $H_0 = 0.7H_K \sim 1.65$ mT, where $\partial C_{11}/\partial|H|$ and $\partial C_{12}/\partial|H|$ reach their maximum values and C_{16} is sufficiently small to be neglected. Additionally, C_{66} is maximized at this field value, while $\partial C_{66}/\partial|H|$ remains negligible. This implies that small changes in the magnetic field around this specific value primarily affect the longitudinal and transverse deformations, with negligible effects on the shear deformations. The values of the primary stiffness tensor components, C_{11}, C_{12}, C_{16} and C_{66}, and their corresponding magnetic sensitivity ($\partial C_{ij}/\partial|H|$) at the magnetic field of H_0 are given in **Table 1**.

We applied a small magnetic perturbation of $\Delta H = 100$ µT over the bias magnetic field of H_0 and estimated the stiffness tensor components for the magnetic field values $H^+ = H_0 + \Delta H/2$ and $H^- = H_0 - \Delta H/2$. We subsequently computed the band structure of the rectangular PnC for the stiffness tensors corresponding to these two field values, given as $\mathbf{C}^+$ and $\mathbf{C}^-$ in Appendix A. **Figure 7** presents the resulting dispersion curves for the PnC mode m_7, plotted near the edge of the first Brillouin zone. The dispersion curves for the other PnC modes (m_1 to m_8) are also computed and displayed in Figure S6 (Supporting Information). From these dispersion curves, the magneto-structural sensitivity $S_{mag-str}$ of each mode was estimated as

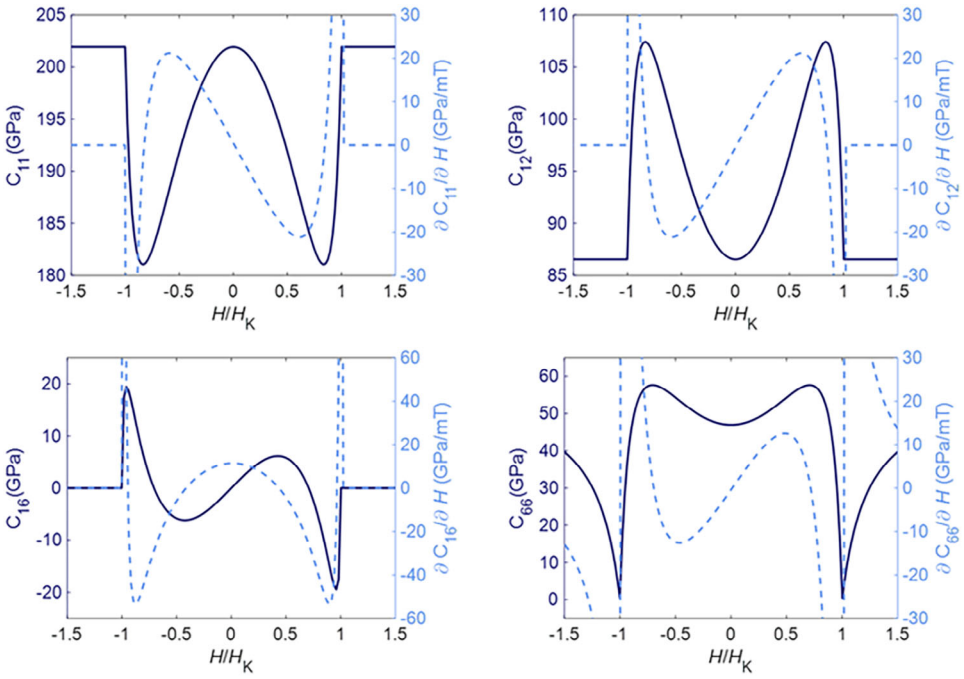

Figure 6. Non-zero magnetic field-dependent components of the FeCoSiB stiffness tensor, i.e., C_{11}, C_{12}, C_{16} and C_{66} (solid dark blue curves), and their derivatives with respect to the applied magnetic field magnitude, $\partial C_{ij}/\partial|H|$ (dashed light blue curves).

Table 1. Calculated values for the primary stiffness tensor components (C_{ij}) and their corresponding magnetic sensitivity ($\partial C_{ij}/\partial|H|$) at the bias magnetic field of $H_0 = 0.7H_K$.

	C_{11}	C_{12}	C_{16}	C_{66}
C_{ij} (GPa)	184	104.4	0.2	57.7
$\frac{\partial C_{ij}}{\partial\|H\|}$ (GPa/mT)	−19.5	19.5	−25.3	2

the phase velocity change Δv in response to a $\Delta H = 100$ μT variation in the magnetic field. The results are presented as $S_{\mathrm{mag-str}}(\frac{\mathrm{m/s}}{\mathrm{mT}})$ in **Table 2**. Generally, the higher-order modes exhibit larger magneto-structural sensitivities due to their flatter profiles, and therefore smaller group velocities, comparing to the lower-order modes. In particular, mode m_7 demonstrates the highest sensitivity to magnetic field variations, with a value of 1588 ($\frac{\mathrm{m/s}}{\mathrm{mT}}$), which is 66 times higher than the sensitivity obtained for a continuous guiding layer without the PnC.

Furthermore, we calculated the resonance frequency of mode m_7 at different magnetic field values around H_0 to analyze the frequency shift of this particular mode under varying magnetic perturbation strengths. As depicted in Figure S7 (Supporting Information), for perturbation strengths in the range of a few hundred μT, the resonance frequency scales linearly and inversely with the applied magnetic field, with a change rate of ≈1 MHz mT^{-1}, shifting to lower frequencies at higher magnetic field values.

For a rectangular PnC with 20 pillars along the *x*-axis, resulting in a total length of $l = 120$ μm, as illustrated in Figure 5, our calculations yield a geometric sensitivity of $S_{\mathrm{geo}} \sim -1.19$ °s m^{-1} at the

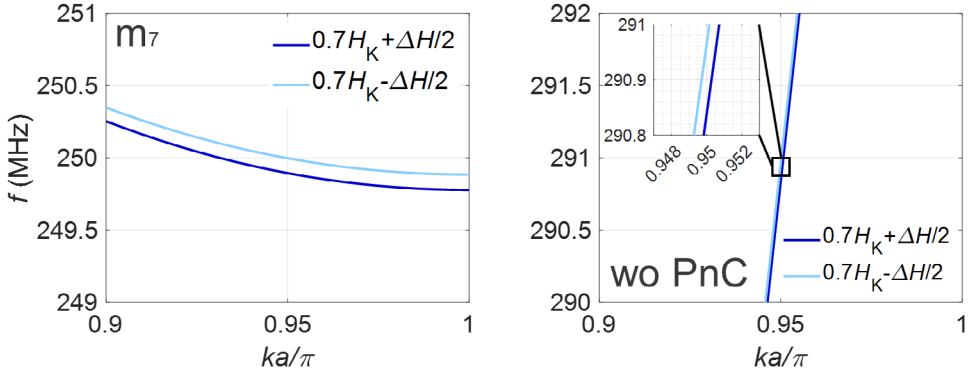

Figure 7. Dispersion curves of the rectangular PnC mode m_7 displayed near the edge of the first Brillouin zone, at $H^+ = 0.7H_K + \Delta H/2$ and $H^- = 0.7H_K - \Delta H/2$, with $\Delta H = 100$ μT. The dispersion curves of the lowest-order mode of a continuous delay line without PnCs are also provided for comparison.

Table 2. Phase velocity change of the rectangular PnC modes m_1 to m_8 per unit change of the applied magnetic field, $S_{mag-str}(\frac{m/s}{mT})$, derived from the data in Figure S6 (Supporting Information).

	m_1	m_2	m_3	m_4	m_5	m_6	m_7	m_8	wo PnC
$S_{mag-str}\left(\frac{m/s}{mT}\right)$	219	220	365	625	563	720	1588	950	23

frequency $f = 250$ MHz and the phase velocity $v \sim 3017$ m s^{-1} for mode m_7. For this mode, an overall sensitivity of $S \sim 1884$ °/mT can be achieved, which is nearly two orders of magnitude greater than that of a continuous delay line of the same dimensions, and over 8 times higher than the sensitivity limits reached in our previous study using PnC structures composed of FeCoSiB pillars,[67] normalized to the delay line length of the present study.

A comprehensive analysis of all geometric parameters, including the periodicity and total length of the PnC, as well as the diameter and thickness of the pillars, and their impact on sensor sensitivity, requires a separate study. Here, we specifically investigate the effects of PnC thickness and periodicity on sensor sensitivity. To assess the impact of PnC thickness, we estimated the magneto-structural sensitivity of the rectangular PnC modes m_1 to m_8 for $a = 6$ µm, $r_p = 1.5$ µm, $q = 2$, and different thicknesses $h = 2.5$, 3, 3.5, 4, 4.5 and 5 µm. The results show that the magneto-structural sensitivity of modes m_1 to m_6 decreases as thickness increases. This reduction is partly due to the fact that the sensitivity of PnC modes scales with their resonance frequency, which shifts to lower values as thickness increases. Normalizing the sensitivity of each mode to its resonance frequency reveals that modes m_1 and m_2 remain unaffected by thickness variations, whereas modes m_3 to m_6 exhibit reduced normalized sensitivity for thicker PnCs due to the weaker interaction of their predominantly in-plane oscillations with the top magnetostrictive layer (Table S1, Supporting Information). Higher-order modes exhibit a different trend, with mode m_7 reaching its maximum sensitivity at $h = 0.5a$ (3 µm), suggesting an optimal thickness for maximizing sensor performance. To evaluate the influence of PnC periodicity, we calculated the normalized magneto-structural sensitivity of modes m_1 to m_8 for $h = 4.5$ µm, $r_p = 1.5$ µm, $q = 2$, and varying lattice constants along the x-axis, $a = 4$, 5, 6, 7 and 8 µm (Table S2, Supporting Information). As the lattice constant a increases, PnC modes shift to lower frequencies, while their normalized magneto-structural sensitivity increases. This increase is attributed to the larger rectangular unit cell area, which results in greater mode interaction with the overlaying magnetostrictive layer. However, a different behavior is observed, particularly in higher-order modes, with mode m_7 reaching its maximum sensitivity at $a = 7$ µm and mode m_8 peaking at $a = 5$ µm. Although higher sensitivity values could be achieved with different geometric parameters, $h = 4.5$ µm and $a = 6$ µm were selected in this study to precisely align PnC mode m_7 with the 250 MHz Rayleigh wave excited by the IDT, while still achieving a relatively high sensitivity.

5. Discussion

The band diagrams illustrate how adjusting the lateral distance between pillars relative to the longitudinal distance, controlled by the coefficient q, affects the band characteristics, such as slope and frequency, in both rectangular and triangular PnCs. However, these two types of PnCs exhibit different responses to changes in q due to their distinct lattice symmetries. In the rectangular PnC, increasing the lateral spacing reduces interactions between the pillars along the y-axis. For sufficiently large values of q (i.e., q>2), this configuration approximates a quasi-1D arrangement of pillars, resulting in degenerate modes at the X-point. As q is reduced, the coupling between the pillars along the y-axis increases, leading to the splitting of these degenerate bands at the X-point (Figure 2). Each mode's sensitivity to changes in q is closely related to its spatial displacement profile. As illustrated in Figure 3, modes in which all pillars along the y-axis oscillate in-phase, i.e., modes 1, 3, 6, and 7, indicated by solid curves, exhibit minimal frequency shifts and slope variations with changes in q. The in-phase oscillation of pillars across the lattice produces consistent coupling between neighboring pillars that remains relatively unaffected by lateral spacing changes. In contrast, modes 2, 4, 5, and 8, indicated by dashed curves, undergo significant frequency shifts and slope changes as q varies. In these modes, neighboring pillars along the y-axis move in opposite directions, making their interaction highly sensitive to lateral spacing. Unlike the rectangular PnC, the band structure of the triangular PnC exhibits greater robustness against variations in q. While slope changes due to variations in q also occur in the triangular PnC, degeneracy is preserved at the X-point for all q values shown in Figure S1 (Supporting Information). This behavior is attributed to the higher inherent symmetry of the triangular lattice compared to the rectangular lattice.

The splitting of degenerate modes at specific q values in the rectangular PnC creates extremely flat bands at the band edges. Compared to the degenerate modes in the triangular PnC, these non-degenerate flat bands yield lower SAW group velocities and stronger resonance effects, as shown in Figures 4 and 5. Moreover, they exhibit relatively larger frequency shifts by altering the lateral spacing of the pillars. Therefore, when rectangular PnCs are precisely designed and fabricated, a PnC mode can be aligned with the desired frequency, i.e., the frequency of the SAW generated by the input IDT. As a result, the SAW propagates through the PnC with an effectively lower velocity, resulting in an increased interaction between the SAW and the magnetostrictive material.

In our study, we achieved a normalized overall sensitivity of ≈15.7 °/mT per 1 µm length of the delay line, which significantly exceeds previously reported values. For example, Kittmann et al. reported a sensitivity of 504 °/mT for a Love-wave SAW magnetic field sensor.[21] With a 3.8 mm long delay line, this corresponds to a normalized sensitivity of 0.13 °/mT·µm. Later, Schell et al. achieved a maximum sensitivity of 2000 °/mT by controlling the magnetic anisotropy of FeCoSiB during the deposition process[74] and developing an exchange bias stack of ferromagnetic and antiferromagnetic layers.[75] With the same delay line length, their

normalized sensitivity is 0.53 °/mT µm. Schmalz et al. reported a sensitivity of 1250 °/mT using a 1.8 mm delay line, resulting in a normalized sensitivity of 0.69 °/mT µm.[76] These comparisons demonstrate that our modeled sensor's sensitivity significantly surpasses existing SAW magnetic field sensors, highlighting the effectiveness of our design.

6. Conclusion

We demonstrate that the sensitivity of a SAW magnetic field sensor can be substantially enhanced by adding PnC structures. The presented design offers an eightfold improvement in overall sensitivity compared to a PnC composed of FeCoSiB pillars and nearly two orders of magnitude improvement over continuous delay line structures. These improvements arise from embedding the pillars within the SiO_2 guiding layer, so that the PnC thickness is equal to that of the guiding layer, rather than being limited by the relatively thin FeCoSiB layer. As predicted in an earlier study,[67] thicker PnCs produce comparatively stronger resonances. Additionally, in the present design, we avoid patterning the FeCoSiB layer in order to increase the interaction volume between the SAW and the magnetostrictive material.

In conclusion, our study highlights the potential of PnC-based designs to advance SAW sensor technology, paving the way for next-generation magnetic field sensors with unprecedented sensitivity and limit of detection. This advancement allows for more precise magnetic field detection across applications from industrial monitoring to medical diagnostics. While the simulation results demonstrate a significant sensitivity enhancement through the integration of PnCs, experimental validation is essential to confirm these findings. Future work will focus on fabricating the proposed sensor design and conducting experimental measurements to verify the predicted sensitivity improvements.

7. Material Parameters

In the model, Silicon was used as the substrate with $E = 169$ GPa, $\upsilon = 0.28$ and $\rho = 2329$ kg m^{-3}[69,77] and $Al_{0.77}Sc_{0.23}N$ as the piezoelectric material, whose material parameters are as follows:[78]

$$\mathbf{C}_{\mathrm{AlScN}} = \begin{pmatrix} 335 & 154 & 119 & 0 & 0 & 0 \\ 154 & 335 & 119 & 0 & 0 & 0 \\ 119 & 119 & 270 & 0 & 0 & 0 \\ 0 & 0 & 0 & 109 & 0 & 0 \\ 0 & 0 & 0 & 0 & 109 & 0 \\ 0 & 0 & 0 & 0 & 0 & 90 \end{pmatrix} \mathrm{GPa} \tag{10}$$

$$\mathbf{e}_{\mathrm{AlScN}} = \begin{pmatrix} 0 & 0 & 0 & 0 & -0.25 & 0 \\ 0 & 0 & 0 & -0.25 & 0 & 0 \\ -0.6 & -0.6 & 2.13 & 0 & 0 & 0 \end{pmatrix} \mathrm{C\,m^{-2}} \tag{11}$$

$$\rho_{\mathrm{AlScN}} = 3278\ \mathrm{kg\ m^{-3}},$$

$$\boldsymbol{\epsilon}_{\mathrm{rAlScN}} = \begin{pmatrix} 9.5 & 0 & 0 \\ 0 & 9.5 & 0 \\ 0 & 0 & 11.5 \end{pmatrix} \tag{12}$$

$$\boldsymbol{\mu}_{\mathrm{rAlScN}} = \begin{pmatrix} 1 & 0 & 0 \\ 0 & 1 & 0 \\ 0 & 0 & 1 \end{pmatrix} \tag{13}$$

where $\mathbf{C}_{\mathrm{AlScN}}$, $\mathbf{e}_{\mathrm{AlScN}}$, and ρ_{AlScN} represent the stiffness tensor, the piezoelectric coupling tensor, and the mass density of $Al_{0.77}Sc_{0.23}N$, respectively, while $\boldsymbol{\epsilon}_{\mathrm{rAlScN}}$ and $\boldsymbol{\mu}_{\mathrm{rAlScN}}$ are the relative electrical permittivity and relative magnetic permeability of $Al_{0.77}Sc_{0.23}N$.

As the magnetostrictive material, FeCoSiB was used with a mass density of $\rho = 7250$ kg m^{-3}, a Young's modulus of $E_0 = 150$ GPa and a Poisson's ratio of $\upsilon = 0.3$ at fixed magnetization.[68] For the magnetoelastic simulations, we set the saturation flux density to $\mu_0 M_s = 1.5$ T and the saturation magnetostriction to $\lambda_s = 35$ ppm.[20,79] The first-order anisotropy constant was set to $K = 1400$ J·m^{-3}.[80] The magnetization curve for the FeCoSiB layer, obtained using the macrospin model,[20] is presented in Figure S8 (Supporting Information).

The stiffness tensors corresponding to the magnetic field values of H^+ and H^+ are given as:

$$\mathbf{C}^{+} = \begin{pmatrix} 183.30 & 105.16 & 86.54 & 0 & 0 & -0.94 \\ 105.16 & 183.30 & 86.54 & 0 & 0 & 0.94 \\ 86.54 & 86.54 & 201.92 & 0 & 0 & 0 \\ 0 & 0 & 0 & 57.69 & 0 & 0 \\ 0 & 0 & 0 & 0 & 57.69 & 0 \\ -0.94 & 0.94 & 0 & 0 & 0 & 57.64 \end{pmatrix} \mathrm{GPa} \tag{14}$$

$$\mathbf{C}^{-} = \begin{pmatrix} 184.81 & 103.66 & 86.54 & 0 & 0 & -1.19 \\ 103.66 & 184.81 & 86.54 & 0 & 0 & 1.19 \\ 86.54 & 86.54 & 201.92 & 0 & 0 & 0 \\ 0 & 0 & 0 & 57.69 & 0 & 0 \\ 0 & 0 & 0 & 0 & 57.69 & 0 \\ -1.19 & 1.19 & 0 & 0 & 0 & 57.61 \end{pmatrix} \mathrm{GPa} \tag{15}$$

Supporting Information

Supporting Information is available from the Wiley Online Library or from the author.

Acknowledgements

This work was funded by the German Research Foundation (Deutsche Forschungsgemeinschaft) via the collaborative research center CRC 1261 "Magnetoelectric Sensors: From Composite Materials to Biomagnetic Diagnostics".

Conflict of Interest

The authors declare no conflict of interest.

Data Availability Statement

The data that support the findings of this study are available from the corresponding author upon reasonable request.

Keywords

magnetic field sensors, magnetostriction, phononic crystals, surface acoustic waves

Received: January 17, 2025
Revised: February 14, 2025
Published online: April 21, 2025

[1] P. Ripka, K. Závěta, *Handbook Magnet. Mater.* **2009**, *18*, 347.
[2] C. P. O. Treutler, *Sens. Actuators A Phys.* **2001**, *91*, 2.
[3] S. S. P. Parkin, C. Kaiser, A. Panchula, P. M. Rice, B. Hughes, M. Samant, S. H. Yang, *Nat. Mater.* **2004**, *3*, 862.
[4] J. Zhai, Z. Xing, S. Dong, J. Li, D. Viehland, *Appl. Phys. Lett.* **2006**, *88*, 62510.
[5] I. R. McFadyen, E. E. Fullerton, M. J. Carey, *MRS Bull.* **2006**, *31*, 379.
[6] M. Díaz-Michelena, *Sensors* **2009**, *9*, 2271.
[7] D. Karnaushenko, D. D. Karnaushenko, D. Makarov, S. Baunack, R. Schäfer, O. G. Schmidt, *Adv. Mater.* **2015**, *27*, 6582.
[8] G. Lin, D. Makarov, O. G. Schmidt, *Lab Chip* **2017**, *17*, 1884.
[9] S. Zuo, J. Schmalz, M. Ö. Özden, M. Gerken, J. Su, F. Niekiel, F. Lofink, K. Nazarpour, H. Heidari, *IEEE Trans. Biomed. Circuits Syst.* **2020**, *14*, 971.
[10] D. Murzin, D. J. Mapps, K. Levada, V. Belyaev, A. Omelyanchik, L. Panina, V. Rodionova, *Sensors* **2020**, *20*, 1569.
[11] E. Elzenheimer, C. Bald, E. Engelhardt, J. Hoffmann, P. Hayes, J. Arbustini, A. Bahr, E. Quandt, M. Höft, G. Schmidt, *Sensors* **2022**, *22*, 1018.
[12] S. M. Hanna, *ITUFF* **1987**, *34*, 191.
[13] V. Polewczyk, K. Dumesnil, D. Lacour, M. Moutaouekkil, H. Mjahed, N. Tiercelin, S. Petit Watelot, H. Mishra, Y. Dusch, S. Hage-Ali, O. Elmazria, F. Montaigne, A. Talbi, O. Bou Matar, M. Hehn, *Phys. Rev. Appl.* **2017**, *8*, 024001.
[14] W. Wang, Y. Jia, X. Xue, Y. Liang, Z. Du, *AIP Adv.* **2018**, *8*, 990884.
[15] X. Liu, B. Tong, J. Ou-Yang, X. Yang, S. Chen, Y. Zhang, B. Zhu, *Appl. Phys. Lett.* **2018**, *113*, 37057.
[16] E. W. Lee, *Rep. Prog. Phys.* **1955**, *18*, 184.
[17] J. D. Livingston, *Phys. Status Solidi* **1982**, *70*, 591.
[18] R. Kellogg, A. Flatau, *J. Intell. Mater. Syst. Struct.* **2007**, *19*, 583.
[19] S. Datta, J. Atulasimha, C. Mudivarthi, A. B. Flatau, *J. Magn. Magn. Mater.* **2010**, *322*, 2135.
[20] B. Spetzler, E. V. Golubeva, R. M. Friedrich, S. Zabel, C. Kirchhof, D. Meyners, J. McCord, F. Faupel, *Sensors* **2021**, *21*, 2022.
[21] A. Kittmann, P. Durdaut, S. Zabel, J. Reermann, J. Schmalz, B. Spetzler, D. Meyners, N. X. Sun, J. McCord, M. Gerken, G. Schmidt, M. Höft, R. Knöchel, F. Faupel, E. Quandt, *Sci. Rep.* **2018**, *8*, 278.
[22] A. Kittmann, C. Müller, P. Durdaut, L. Thormählen, V. Schell, F. Niekiel, F. Lofink, D. Meyners, R. Knöchel, M. Höft, J. McCord, E. Quandt, *Sens. Actuators A Phys.* **2020**, *311*, 111998.
[23] J. Su, F. Niekiel, S. Fichtner, C. Kirchhof, D. Meyners, E. Quandt, B. Wagner, F. Lofink, *J. Micromech. Microeng.* **2020**, *30*, 075009.
[24] P. Durdaut, C. Müller, A. Kittmann, V. Schell, A. Bahr, E. Quandt, R. Knöchel, M. Höft, J. McCord, *Sensors* **2021**, *21*, 5631.
[25] J. M. Meyer, V. Schell, J. Su, S. Fichtner, E. Yarar, F. Niekiel, T. Giese, A. Kittmann, L. Thormählen, V. Lebedev, S. Moench, A. Žukauskaitė, E. Quandt, F. Lofink, *Sensors* **2021**, *21*, 8166.
[26] H. Greve, E. Woltermann, R. Jahns, S. Marauska, B. Wagner, R. Knöchel, M. Wuttig, E. Quandt, *Appl. Phys. Lett.* **2010**, *97*, 122342.
[27] S. Zabel, J. Reermann, S. Fichtner, C. Kirchhof, E. Quandt, B. Wagner, G. Schmidt, F. Faupel, *Appl. Phys. Lett.* **2016**, *108*, 30497.
[28] S. Salzer, V. Röbisch, M. Klug, P. Durdaut, J. McCord, D. Meyners, J. Reermann, M. Höft, R. Knöchel, *IEEE Sens. J.* **2018**, *18*, 596.
[29] M. Yamaguchi, M. Naoe, H. Kogo, *IEEE Trans. Magn.* **1980**, *16*, 916.
[30] Y. Q. Fu, J. K. Luo, N. T. Nguyen, A. J. Walton, A. J. Flewitt, X. T. Zu, Y. Li, G. McHale, A. Matthews, E. Iborra, H. Du, W. I. Milne, *Prog. Mater. Sci.* **2017**, *89*, 31.
[31] Y. Takagaki, P. V. Santos, E. Wiebicke, O. Brandt, H. P. Schönherr, K. H. Ploog, *Appl. Phys. Lett.* **2002**, *81*, 2538.
[32] G. Piazza, V. Felmetsger, P. Muralt, R. H. Olsson, R. Ruby, *MRS Bull.* **2012**, *37*, 1051.
[33] U. C. Kaletta, P. V. Santos, D. Wolansky, A. Scheit, M. Fraschke, C. Wipf, P. Zaumseil, C. Wenger, *Semicond. Sci. Technol.* **2013**, *28*, 065013.
[34] T. Aubert, J. Bardong, O. Legrani, O. Elmazria, M. Badreddine Assouar, G. Bruckner, A. Talbi, *J. Appl. Phys.* **2013**, *114*, 014505.
[35] R. M. R. Pinto, V. Gund, R. A. Dias, K. K. Nagaraja, K. B. Vinayakumar, *J. Microelectromech. Syst.* **2022**, *31*, 500.
[36] S. Fichtner, N. Wolff, G. Krishnamurthy, A. Petraru, S. Bohse, F. Lofink, S. Chemnitz, H. Kohlstedt, L. Kienle, B. Wagner, *J. Appl. Phys.* **2017**, *122*, 035301.
[37] J. Casamento, C. S. Chang, Y. T. Shao, J. Wright, D. A. Muller, H. Xing Grace, D. Jena, *Appl. Phys. Lett.* **2020**, *117*, 112101.
[38] L. Dreher, M. Weiler, M. Pernpeintner, H. Huebl, R. Gross, M. S. Brandt, S. T. B. Goennenwein, *Phys. Rev. B Condens. Matter Mater. Phys.* **2012**, *86*, 134415.
[39] X. Li, D. Labanowski, S. Salahuddin, C. S. Lynch, *J. Appl. Phys.* **2017**, *122*, 43904.
[40] Y. Nozaki, S. Yanagisawa, *Electric. Eng. Japan* **2018**, *204*, 3.
[41] D. A. Bas, P. J. Shah, M. E. McConney, M. R. Page, *J. Appl. Phys.* **2019**, *126*, 114501.
[42] R. Sasaki, Y. Nii, Y. Iguchi, Y. Onose, *Phys. Rev. B* **2017**, *95*, 020407.
[43] R. Verba, V. Tiberkevich, A. Slavin, *Phys. Rev. Appl.* **2019**, *12*, 054061.
[44] M. Xu, K. Yamamoto, J. Puebla, K. Baumgaertl, B. Rana, K. Miura, H. Takahashi, D. Grundler, S. Maekawa, Y. Otani, *Sci. Adv.* **2020**, *6*, 32.
[45] P. J. Shah, D. A. Bas, I. Lisenkov, A. Matyushov, N. X. Sun, M. R. Page, *Sci. Adv.* **2020**, *6*, eabc5648.
[46] C. Chen, L. Han, P. Liu, Y. Zhang, S. Liang, Y. Zhou, W. Zhu, S. Fu, F. Pan, C. Song, *Adv. Mater.* **2023**, *35*, 2302454.
[47] E. Yablonovitch, *JOSA B* **1993**, *10*, 283.
[48] T. F. Krauss, R. M. De La Rue, S. Brand, *Nature* **1996**, *383*, 699.
[49] S. Noda, K. Tomoda, N. Yamamoto, A. Chutinan, *Science* **2000**, *289*, 604.
[50] Y. Akahane, T. Asano, B. S. Song, S. Noda, *Nature* **2003**, *425*, 944.
[51] P. Lalanne, C. Sauvan, J. P. Hugonin, *Laser Photon Rev.* **2008**, *2*, 514.
[52] S. Hu, S. M. Weiss, *ACS Photonics* **2016**, *3*, 1647.
[53] J. D. Joannopoulos, M. Soljačić, E. Ippen, M. Ibanescu, S. Fan, S. G. Johnson, *JOSA B* **2002**, *19*, 2052.
[54] M. Dorseth, S. Bourouaine, J. C. Perez, T. Xie, Z. Wu, T. J. Foutz, N. K. Walia, K. Seki, T. F. Krauss, *J. Phys. D Appl. Phys.* **2007**, *40*, 2666.
[55] T. Baba, *Nat. Photonics* **2008**, *2*, 465.
[56] D. Threm, Y. Nazirizadeh, M. Gerken, *J. Biophoton.* **2012**, *5*, 601.
[57] R. Gao, Y. Jiang, S. Abdelaziz, *Opt. Lett.* **2013**, *38*, 1539.
[58] Y. N. Zhang, Y. Zhao, T. Zhou, Q. Wu, *Lab Chip* **2017**, *18*, 57.
[59] A. Khelif, A. Adibi, *Phononic Crystals: Fundamentals and Applications*, Springer, Berlin **2015**.
[60] M. Krawczyk, D. Grundler, *J. Phys.: Condens. Matter* **2014**, *26*, 123202.
[61] S. Tamura, D. C. Hurley, J. P. Wolfe, *Phys. Rev. B* **1988**, *38*, 1427.
[62] V. Laude, M. Wilm, S. Benchabane, A. Khelif, *Phys. Rev. E Stat. Nonlin. Soft Matter Phys.* **2005**, *71*, 036607.
[63] S. Benchabane, A. Khelif, J. Y. Rauch, L. Robert, V. Laude, *Phys. Rev. E Stat. Nonlin. Soft Matter Phys.* **2006**, *73*, 065601.

[64] A. Khelif, B. Aoubiza, S. Mohammadi, A. Adibi, V. Laude, *Phys. Rev. E Stat. Nonlin. Soft Matter Phys.* **2006**, *74*, 046610.
[65] M. Badreddine Assouar, M. Oudich, *Appl. Phys. Lett.* **2011**, *99*, 123505.
[66] M. Oudich, N. J. Gerard, Y. Deng, Y. Jing, M. Oudich, N. J. Gerard, Y. Deng, Y. Jing, M. O. Institut, J. Lamour, *Adv. Funct. Mater.* **2023**, *33*, 2206309.
[67] M. Samadi, J. Schmalz, J. M. Meyer, F. Lofink, M. Gerken, *Micromachines* **2023**, *14*, 2130.
[68] C. Cordier, C. Dolabdjian, *IEEE Sens. J.* **2023**, *23*, 2014
[69] J. Schmalz, E. Spetzler, J. McCord, M. Gerken, *Sensors* **2023**, *23*, 5012.
[70] J. Yang, *An Introduction to the Theory of Piezoelectricity*, Springer, Cham **2018**, 53–79.
[71] IEEE Standard on Magnetostrictive Materials: Piezomagnetic Nomenclature, *IEEE Trans. Sonics Ultrasonics* **1973**, *20*, 67.
[72] *COMSOL Multiphysics® v. 6.2. COMSOL AB* Stockholm, Sweden, http://www.comsol.com.
[73] A. Khelif, Y. Achaoui, S. Benchabane, V. Laude, B. Aoubiza, *Phys. Rev. B – Condens. Matter Mater. Phys.* **2010**, *81*, 214303.
[74] V. Schell, C. Müller, P. Durdaut, A. Kittmann, L. Thormählen, F. Lofink, D. Meyners, M. Höft, J. McCord, E. Quandt, *Appl. Phys. Lett.* **2020**, *116*, 7.
[75] V. Schell, E. Spetzler, N. Wolff, L. Bumke, L. Kienle, J. McCord, E. Quandt, D. Meyners, *Sci. Rep.* **2023**, *13*, 8446.
[76] J. Schmalz, A. Kittmann, P. Durdaut, B. Spetzler, F. Faupel, M. Höft, E. Quandt, M. Gerken, *Sensors* **2020**, *20*, 3421.
[77] J. L. Gugat, M. C. Krantz, M. Gerken, *IEEE Trans. Magn.* **2013**, *49*, 5287.
[78] M. A. Caro, S. Zhang, T. Riekkinen, M. Ylilammi, M. A. Moram, O. Lopez-Acevedo, J. Molarius, T. Laurila, *J. Phys.: Condens. Matter* **2015**, *27*, 245901.
[79] A. Ludwig, E. Quandt, *IEEE Trans. Magn.* **2002**, *38*, 2829.
[80] B. Spetzler, E. V. Golubeva, C. Müller, J. McCord, F. Faupel, *Sensors* **2019**, *19*, 4769.